Simulations of the mechanical properties of crystalline, nanocrystalline, and amorphous SiC and Si

V. I. Ivashchenko,[1] P. E. A. Turchi,[2] and V. I. Shevchenko[1]
[1]*Institute of Problems of Materials Science, NAS of Ukraine, Krzhyzhanovsky Strasse 3, 03142 Kyiv, Ukraine*
[2]*Lawrence Livermore National Laboratory (L-372), P.O. Box 808, Livermore, California 94551, USA*
(Received 22 May 2006; revised manuscript received 25 September 2006; published 14 February 2007)

Molecular-dynamics simulations of crystalline (c), nanocrystalline (nc), and amorphous (a) silicon carbides and silicon were carried out to investigate their vibrational and mechanical properties. The atomic configurations, vibrational spectra, and stress-strain curves were calculated at room temperature. In the case of the nanocrystalline structures, these characteristics were analyzed as functions of grain size. Young's and bulk modul and yield and flow stresses were determined from uniaxial deformation of samples under periodic boundary constraints and from experiments on rod extension. For silicon carbides, Young's modulus and flow stress decrease in the sequence "c-nc-a," and with decreasing grain size, which is attributed to a weakening of the Si–C bonds in the amorphous matrix. The enhancement of the strength properties of the homopolar nc–Si structures is attributed to their deformation anisotropy. The calculated vibrational spectra and Young's moduli are in rather good agreement with the corresponding experimental characteristics.

DOI: 10.1103/PhysRevB.75.085209 PACS number(s): 61.43.Dq, 71.15.Pd, 71.23.Cq

I. INTRODUCTION

Amorphous (*a*) and nanocrystalline (nc) silicon carbide and pure silicon are remarkably interesting materials, both from fundamental and technological points of view, for their numerous optoelectronic[1–3] and tribological applications.[3–5] They combine not only interesting optical and electrical properties but also excellent micromechanical characteristics that make them suitable for microelectromechanical systems (MEMS) applications.[6] MEMS represent microcomponents and microdevices that have been developed using lithography based and other techniques, with physical dimensions ranging from a couple of microns to a few thousand microns. Very few studies on such systems have been carried out at the nanoscale level because of the difficulties in fabricating small-scale test specimens, and also because of the problems associated with measuring ultrasmall physical phenomena in such experiments.[6] Therefore, theoretical investigations of the strength properties of SiC- and Si-based nanosized structures take on special significance.

a- and nc-Si and -SiC are mainly obtained as thin films that are usually prepared by chemical vapor deposition (CVD), plasma-enhanced CVD (PECVD), electron-cyclotron resonance (ECR) CVD, magnetron sputtering, and pulsed-laser deposition.[3] Since SiC-based materials show the most promising strength properties, we will mainly focus on SiC structures in our investigation. To our knowledge, a few studies on the tribological behavior,[4,5] nanohardness (*H*), Young's modulus (*E*),[4,5,7–12] and phase transformation under nanoindentation[13] of amorphous and nanostructured thin films have been undertaken. Hydrogenated PECVD SiC films deposited at temperatures higher than 300 °C exhibit good abrasive wear resistance at comparatively low values of *H* and *E*.[5] It has been reported for ECR-PECVD films that enhancement in the elastic modulus correlates well with an increase in film density.[7] For unhydrogenated films, not only the hardness varies with the film composition and exhibits a maximum value at equiatomic composition, but at a given composition, it can also be maximized by reducing the hydrogen content in the films.[8] Young's modulus was found to increase with deposition temperature, as a result of hydrogen desorption from the films.[9] In the case of unhydrogenated PVD SiC films,[10–12] an enhancement of strength properties is attributed to film densification. A constant-plus-linear dependence of both the *H* and *E* values of *a*-SiC films on their Si–C bond density has been established, regardless of the film composition or the deposition procedure.[11,12] There are several investigations of the elastic properties of nanocrystalline silicon (nc-Si) bulk materials[6] that show that their nanohardness and elastic modulus are strongly influenced by the microstructure and the nature of the bonding.

The atomic structure of *a*-SiC has been thoroughly studied by using various theoretical procedures, including molecular-dynamics (MD) simulations based on a first-principles pseudopotential method,[14,15] the empirical Tersoff potential,[16,17] and a tight-binding model.[18] State of the art procedures in this field can be found elsewhere.[14,16–18] The theoretical studies on the structural and vibrational properties of *a*-Si were reviewed in Ref. 19. The structure and vibrational spectra of nc-Si have been studied theoretically to a lesser extent,[20–23] whereas these properties for nc-SiC are still unknown. So far, comprehensive theoretical studies on the strength properties of crystalline, amorphous, and nanocrystalline SiC and Si are still lacking.

In this work, we aim at filling this gap by studying the structural, vibrational, and strength properties of these materials. The goals of the present investigation were to generate samples of crystalline, nanocrystalline, and amorphous SiC and Si by using MD simulations, to calculate their vibrational spectra and, subsequently, to investigate the strength properties of the generated samples as functions of their microstructure. For this purpose, we use two approaches: uniaxial deformation [with periodic boundary constraints (PBCs) and rod extension (without PBC)]. Based on the simulation results, the possible mechanisms of evolution of the microstructure and strength properties of the SiC and Si

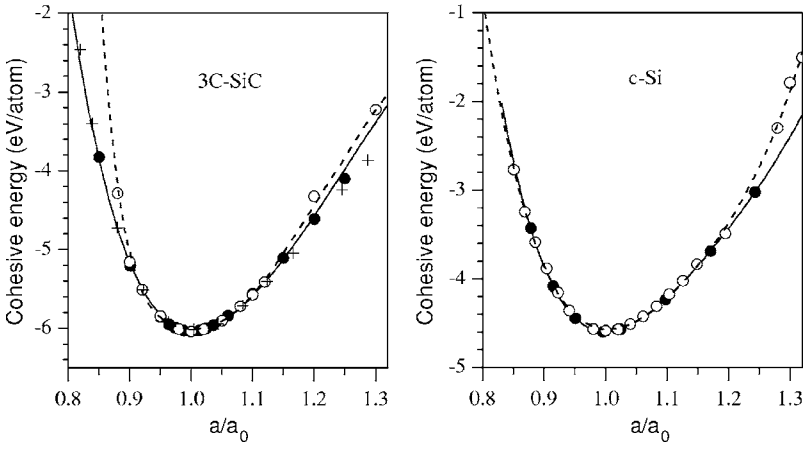

FIG. 1. Cohesive energies of 3C-SiC and c-Si as functions of the normalized lattice constant (where a_0 is the equilibrium lattice constant). The FLAPW results are represented by full circles and the solid line, the data of Tang and Yip (Ref. 28) by crosses, and our results of MD simulations by open circles and the dashed line.

structures under deformation are discussed. In the case of the nanocrystalline structures, strength properties are analyzed as functions of grain size.

The paper is organized as follows. In Sec. II, we discuss the setup of the nanocrystalline model systems and the simulation methods. The simulation results on the structural and vibrational properties are summarized and discussed in Sec. III. The mechanical properties of the systems under consideration are analyzed in Sec. IV. Section V is devoted to the examination of the atomic configurations of the systems under deformation, and Sec. VI contains the main conclusions.

II. SIMULATION SETUP

As mentioned above, our MD simulations is based on the modified Tersoff potential,[16] with the parameters of the C-C interactions determined from diamond. However, since this potential has been fitted to the corresponding equilibrium properties, in the case of significant uniaxial strains, its predictive capability should be discussed in more detail. For Si, a review has been devoted to an analysis of the six most frequently used empirical potentials.[24] In the case of SiC, in contrast to unary systems such as Si or C, an additional interaction between Si and C needs to be taken into account. Two original empirical potentials[16,25,26] have been developed. Later, the Tersoff formalism has been improved by including volume-dependent cutoff distances[27,28] and by matching the short-range interactions to first-principles calculations.[29] To investigate the chemically ordered SiC structures, an interatomic potential that involves both two-body and three-body terms has been suggested.[30,31] The interatomic potential schemes[27–29] describe fairly well the homogeneous compression or expansion, but are not as convenient for MD simulations of uniaxial deformation. On the other hand, the potential[30] is not suitable for modeling chemically disordered SiC materials that are *a*-SiC films prepared with magnetron sputtering, laser ablation, or ion-induced amorphization.[32] Therefore, we decided in favor of the second version of the Tersoff potential.[16] At the same time, the potential has been modified by varying the parameter χ_{SiC} to have a Young modulus for 3C-SiC as close as possible to the experimental value. In Fig. 1, we compare the cohesive energies of 3C-SiC and crystalline silicon (*c*-Si) as functions of the lattice parameter (a) determined from first-principles calculations based on the full potential linearized augmented-plane-wave (FLAPW) method and from MD simulations based on the modified Tersoff potential. For the sake of comparison, the results from other studies[27,28] are also shown. One can see that for large lattice constants a, the modified Tersoff potential overestimates the first-principles results, whereas the potential scheme[27,28] slightly underestimates them. In the case of 3C-SiC, the modified Tersoff potential also strongly overestimates the FLAPW data for the materials under compression. Judging from the results presented in Fig. 1, the potential is expected to overestimate the melting temperature and the deformation effects in both compounds. However, the actual validity of the potential can only be verified by comparison with experiment. As a first validation test for this procedure, we show in Fig. 2 the temperature variation of the lattice constant of 3C-SiC up to 1500 K at zero pressure. The linear temperature coefficients determined from the experimental[33] and calculated curves are 1.4×10^{-6} and 2.4×10^{-6} nm/K, respectively, which means that the potential produces a rather acceptable thermal expansion coefficient. It will be shown below that the potential is also capable of providing quite accurate results for Young's modulus, Poisson's ratio, and the nanohardness of the SiC and Si structures under consideration. Using MD simulations based on the Tersoff potential[16] in the Andersen

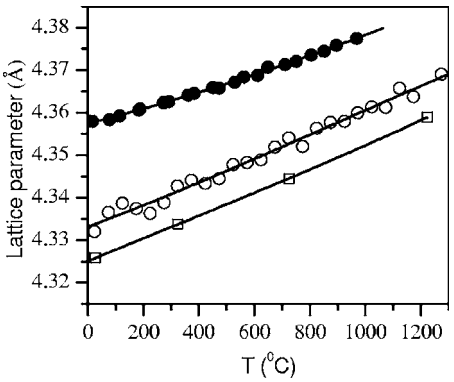

FIG. 2. Lattice constant of 3C-SiC versus temperature. Experimental results (Ref. 33) are represented by full circles, the results of Tang and Yip (Ref. 28) by open square, and the results of the present work by open circles.

constant number-of-particles–pressure–temperature (*NPT*) ensemble, we have generated 4096-atom samples of 3C-SiC, *a*-SiC, and nc-SiC. The nanostructured nc-SiC1, nc-SiC8, and nc-SiC64 samples contain 1, 8, and 64 spherical 3C-SiC nanocrystallites with diameters of 3.5, 1.8, and 0.9 nm, respectively. The nanocrystalline structures have the same initial crystalline fractions equal to ~50%. The crystalline fraction increased after cooling. The 3C-SiC sample was generated by means of an equilibration of the corresponding crystal at 300 K during 20 ps. To generate the nanocrystalline samples, first the spherical-like touching clusters were singled out, randomly reoriented, and then fixed. Two types of samples were also generated with the same (100) and (110) crystallite orientations. The systems were heated to 8000 K, equilibrated during 20 ps at this temperature, and then quenched to 1600 K with a cooling rate of about 10^{13} K/s. At this temperature, the nanocrystalline samples were allowed to evolve for 10 ps without freezing the nanoclusters, and then cooled to 300 K. Finally, the samples were equilibrated at 300 K for 20 ps. The amorphous sample was generated with the same procedure, except that *a*-SiC did not contain any nanoclusters, and cooling was carried out in a single step. The equilibrium lattice parameters (a_0) and the bulk modulus (B) were determined from the Murnaghan equation of state[34] by varying the sample volume during MD simulations at 300 K in the constant number-of-particles–volume–temperature (NVT) ensemble with a time step of 1.0 fs.

Similar calculations were carried out for *c*-Si, nc-Si, and *a*-Si. The nanocrystalline nc-Si1, nc-Si8, and nc-Si64 samples, with spherical crystallites with diameters of 4.3, 2.2, and 1.1 nm, respectively, were generated by cooling these structures with fixed *c*-Si nanoclusters previously heated up to 4000 K. As for the remaining steps, the simulation procedure is similar to what has been described above. For both the SiC and Si structures, simulations started with the systems at a temperature well above the melting point. Consequently, the systems could lose any structural memory from the corresponding crystalline phase after annealing.[14,16]

In order to verify the stability of our final samples, we have additionally equilibrated the final nc-Si8 and nc-SiC8 samples at various time intervals up to 200 ps at 300 K, and found that they are quite thermodynamically stable at room temperature.

To determine the stress-strain curves, we used the following two approaches. In the first approach, at each time interval (800 MD steps that correspond to approximately 0.8 ps), the system was uniaxially elongated by applying a negative external pressure in the x direction according to $P_x=-n\Delta P$, where n is the number of time steps and ΔP is a small pressure increment presently chosen to be $\Delta P=0.008$ Mbar. The simulations were carried out at 300 K in the *NPT* ensemble with PBC and by maintaining the bulk modulus B constant. During each time interval, the atomic forces were relaxed, and therefore the normal and lateral dimensions were optimized. Such a procedure corresponds to a strain rate of approximately 10^{10} s^{-1}. The x component of the atomic stress tensor was calculated and averaged over a region of space to obtain a macroscopic stress field as described in Ref. 35. In the second approach, we considered rodlike samples that underwent uniaxial extension along the (100) axis of the cubic supercells at 300 K without PBC. The atoms on the [100] plane were shifted in the opposite direction by 0.05 Å and then were fixed during subsequent MD evolution. The extension rate (v) was 2, 50, and 100 m/s. We performed MD simulations of the rod extension of a 1000-atom *c*-Si sample using different time steps up to 5 fs, and found that the maximum deviation in the failure strength was about 4%, whereas the Young modulus was practically constant. The main maximum in the strain-stress curves became slightly sharper with an increase in the time step. Based on these findings, we infer that the time steps in the range of 1–3 fs provide quite acceptable results. Therefore, we have used the slightly higher time step of 2.5 fs in the MD simulations of the low-rate rod extension to save simulation time. Further in this paper, we will distinguish between the bulk and rodlike samples that were used in the stress-strain tests investigated with the first and second approaches, respectively.

The effect of sample size on the character of deformation was tested on the *c*-Si rodlike samples with sides $a_x \neq a_y = a_z$ in the range of 21.72–54.3 Å and for various a_z/a_x ratios. It was found that a reduction in sample size leads to insignificant smearing of the main maximum in stress-strain curves. For the rest, the stress-strain dependences are weakly sensitive to sample size. We also generated an 8000-atom nc-SiC125 sample (like the nc-SiC64 one) that contains 125 spherical 3C-SiC nanocrystallites with a diameter of 0.9 nm, and found that the maximum deviation between the stress-strain curves of these bulk samples did not exceed 2%. This point is discussed below in more detail.

Young's modulus (E) is given by the slope of the stress-strain curve in the linear region. When calculating Young's modulus from simulation results, a compromise has to be made between collecting enough data points for a reliable fit and selecting data associated with the linear region. This linear region is specific for each system. The limiting value of these curves corresponds to the yield stress. The accuracy of the determination of Young's modulus and yield stress was ±0.4 GPa. The stress continues to rise after the yield point has been reached until it reaches a plateau (the flow stress σ_{flow}) and becomes constant or slightly decreases. Poisson's ratio (ν) was estimated from the expression[36]

$$\nu = \frac{1}{2}\left(1 - \frac{E}{3B}\right). \tag{1}$$

The vibrational density of states for the undeformed samples was calculated from the Fourier transform of the velocity autocorrelation function. The description of this computational procedure can be found elsewhere.[20]

For the present *ab initio* investigation of 3C-SiC and *c*-Si, nonrelativistic band structure calculations within the local-density approximation of density-functional theory were carried out using the FLAPW method[37] for the face-centered lattice. The semicore states were considered as valence states, while the core states were treated as atomiclike states. The wave functions were expanded into a set of augmented plane waves with wave vectors up to $kR_s=8.0$, where R_s is the smallest radius of the muffin-tin spheres. For 3C-SiC, a

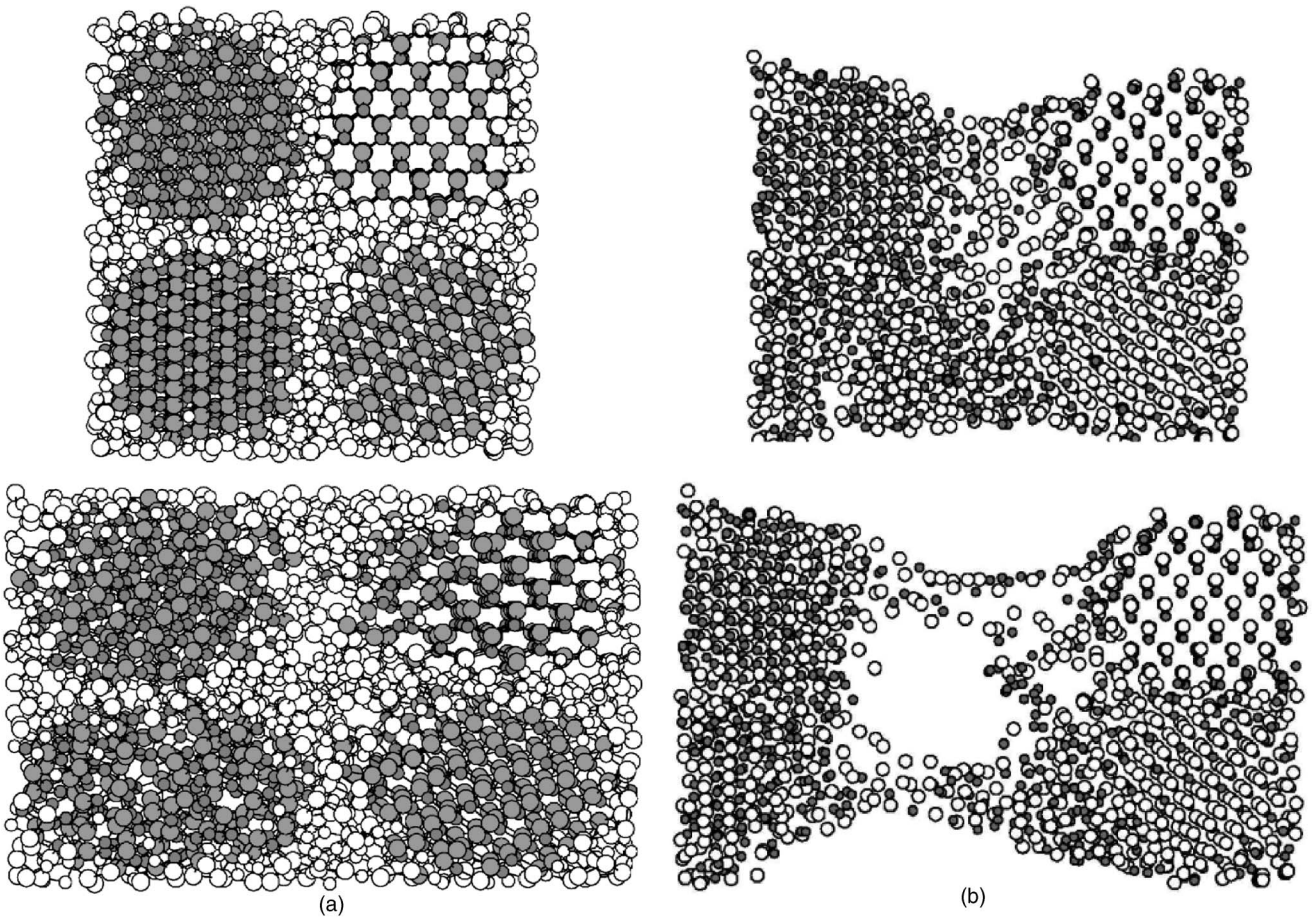

FIG. 3. Cross sections of the atomic configurations of the nc-SiC8 samples under different stages of strain. (a) bulk samples under uniaxial strain (top: $\epsilon=0$; bottom: $\epsilon=0.42$). (b) rod samples under uniaxial tension (top: $\epsilon=0.28$; bottom: $\epsilon=0.45$).

ratio $R_{Si}/R_C=1.1$ was selected. Inside these spheres, the potentials and the charge densities were expanded in spherical harmonics up to $l=8$. The magnitude of the largest vector in charge density Fourier expansion was 14. The criterion of convergence for the total energy was 0.1 mRy/f.u.. The generalized gradient approximation for the exchange-correlation potential was employed.[38] For the k integration, the modified tetrahedron method[39] was used throughout. We selected a minimal set of k points in the irreducible wedge of the Brillouin zone that guarantees changes in the total energy by no more than about 1 mRy/f.u. by further increasing the number of wave vectors. The selected conditions for the FLAPW calculations provide lattice constants of 4.38 Å (3C-SiC) and 5.48 Å (c-Si) and bulk moduli of 211 GPa (3C-SiC) and 88.6 GPa (c-Si).

III. ATOMIC STRUCTURE AND VIBRATIONAL SPECTRA

In Fig. 3, we show the atomic configurations of the nc-SiC8 samples at different stages of the uniaxial deformation and rod extension. In the undistorted sample, the randomly oriented spherical nanocrystallites are clearly seen. This and other nanocrystalline samples represent the 3C-SiC (c-Si) crystallites (grains) embedded in an a-SiC (a-Si) matrix. We also note the grain boundary that corresponds to an aggregate of atoms located in the outer region of a spherical crystallite between R_0 and $R_0-\Delta R$, where R_0 is the radius of the spherical crystallite and $\Delta R=1.5$ Å. Such a value of ΔR provides a strictly fourfold coordination for all atoms belonging to a grain. The grain boundaries and amorphous matrix exhibit different configurations depending on crystallite orientations.

One of the characteristics of the structural transformations in the "c-nc1-nc8-nc64-a" sequence is reflected in the pair-correlation function (PCF). For the SiC and Si systems, the PCFs are displayed in Fig. 4. Given the fact that the crystalline fraction in all the generated nanostructured samples is constant, two main features should be noted. First, all the peaks widen when approaching the amorphous state, and this can be attributed to an enhancement of the topological disorder of the amorphous matrix. Second, for silicon carbides, in the aforementioned sequence, the peak related to the Si-C nearest-neighbor pair correlation decreases, and this points to a decrease in chemical order. The comparison of the calculated PCF with the experimental curves shows that the theoretical a-SiC sample has lower chemical ordering than as-irradiated a-SiC.[40] The structure of a-SiC generated in the present work is very close to that obtained as a result of first-principles MD simulations.[14] In particular, the percentage of homonuclear bonds formed with Si and C is 56% and 48%, respectively, which is comparable to the values of 53% and 45% from *ab initio* MD,[14] respectively. For a-Si, both

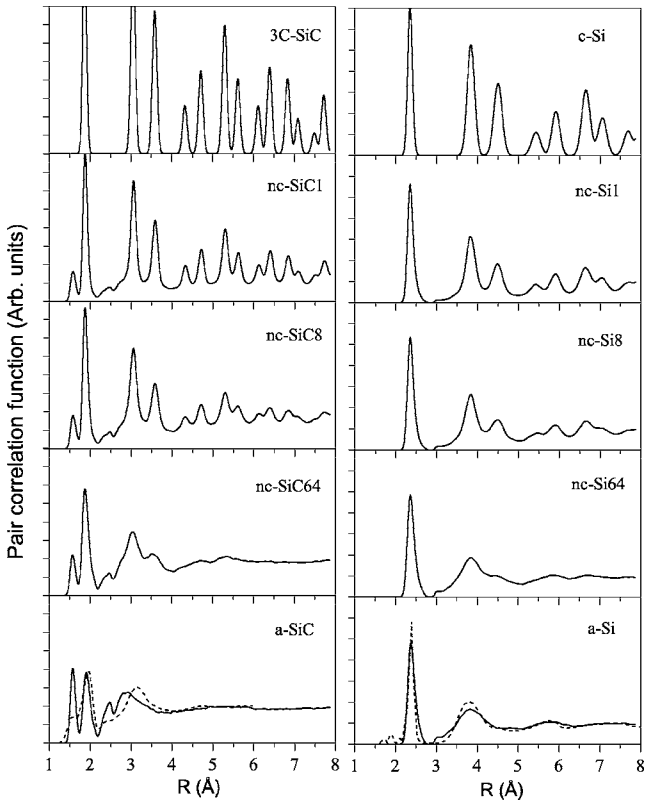

FIG. 4. Pair-correlation function (PCF) of crystalline, nanocrystalline and amorphous structures described in the text. For comparison, the experimental PCF of *a*-SiC (Ref. 40) and *a*-Si (Ref. 41) are also shown (dashed line).

the calculated and experimental curves agree rather well.

The vibrational density of states (VDOS) of the SiC and Si systems is shown in Fig. 5. For the sake of comparison, the experimental phonon densities of states are also presented. It is seen that our approach slightly overestimates the energies of the transverse-optical vibrations. In most cases, the information on vibrational properties is extracted from Raman spectroscopy and, to a lesser extent, from infrared spectroscopy. There are several studies devoted to the determination of Raman spectra for the SiC structures.[13,44–47] For 3C-SiC, the sharp peak near 790 cm^{-1} and the weak peak around 970–975 cm^{-1} are assigned to the TO and LO (T, transverse; L, longitudinal; A, acoustic; O, optical) vibrational modes, respectively.[13,44] These two peaks with weak modifications were also observed in the Raman spectra of nc-SiC.[45–47] Based on the data on Raman spectroscopy of *a*-SiC, the broad bands at 980, 810, and 550 cm^{-1} and the band at lower than 500 cm^{-1} were assigned to the LO, TO, LA, and TA vibrational modes, respectively.[13] Given these results, we can assign the shoulder at 965 cm^{-1}, the prominent peak at 806 cm^{-1}, and the two peaks around 580 and 400 cm^{-1} in the VDOS of 3C-SiC (cf. Fig. 5) to the LO, TO, LA, and TA vibrations, respectively. From Fig. 5, it is clearly seen that in the sequence "3C-SiC–nc-SiC(1–8–64)–*a*-SiC," the band around 500 cm^{-1} increases and the vibrations with wave numbers higher than 1000 cm^{-1} are enhanced, which imply an enhancement of the Si–Si and C–C bond vibrations, respectively.[47,48] The shift towards lower wave numbers of

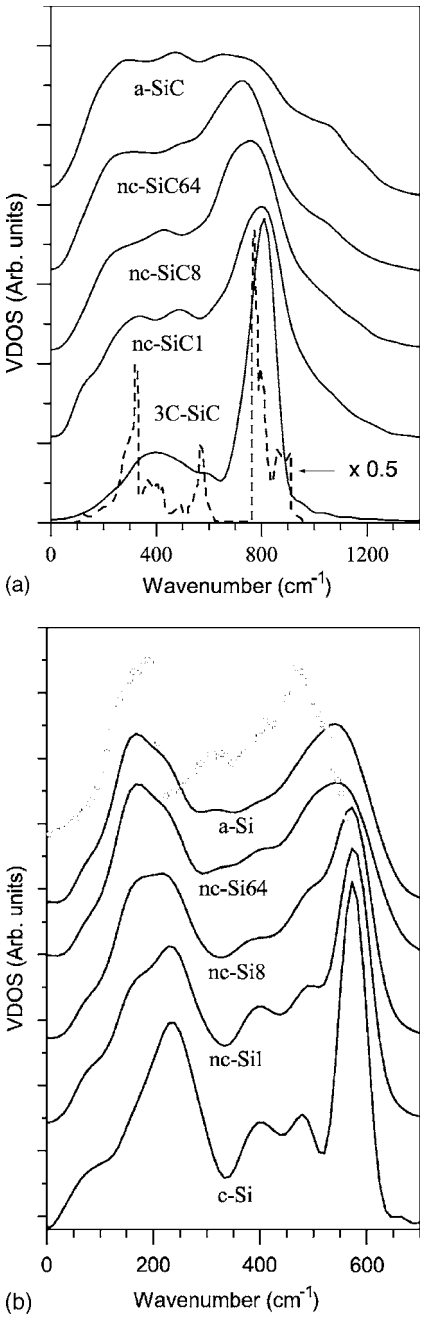

FIG. 5. Calculated vibrational density of states (VDOS) of *c*-, nc- and *a*-SiC and Si. The experimental spectra of 3C-SiC (dashed line) (Ref. 42) and *a*-Si (open circles) (Ref. 43) are also shown.

the peak associated with the TO-like vibrations is caused by a weakening of the Si–C vibrations. The established regularities in the VDOS are consistent with the changes in the pair-correlation function of the SiC samples (cf. Fig. 4) and point to a lowering of chemical order in the sequence mentioned above.

In the case of the VDOS of *c*-Si (cf. Fig. 5), the peaks near 230 (175), 398 (340), 470 (420), and 570 (510–520) cm^{-1} correspond to the TA, LA, LO, and TO vibrational modes, respectively (in parentheses are the corresponding experimental values[13,20,49]). The comparison of these results with the experimental Raman spectra for *c*-Si

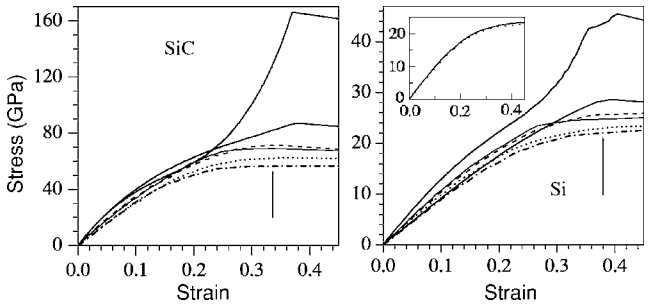

FIG. 6. Stress-strain curves for bulk SiC and Si samples. In the direction along the vertical arrows, the curves are arranged as follows: *a*-nc64-nc8-nc1-*c*(100)-*c*(110). In the inset, the results of the comparison of the stress-strain curves between the nc-SiC64 and nc-SiC125 samples are shown.

shows that our procedure slightly overestimates the TO phonon peak energy. However, as will be shown below, it reproduces correctly the relative changes in the phonon spectra depending on the sample structure. In the sequence "*c*-Si–nc-Si1–nc-Si8," the positions of the main peaks are weakly sensitive to the sample structure. Similar results were obtained for paracrystalline silicon.[20] Appreciable shifts of the peaks towards low wave numbers occur when approaching the nc-Si64 (with a grain size of about 1.1 nm) and *a*-Si samples. A low-energy shift of the TO peak when going from *c*-Si to *a*-Si was detected both in the experimental and theoretical investigations.[13,19] The broadening of the VDOS peaks and their shift to lower wave numbers when approaching the amorphous state may be caused by an increase in the fraction of abnormally coordinated atoms with weak bonds in the amorphous matrix. We also note a peculiar ratio between the intensities of the TA and TO peaks, I_{TA}/I_{TO}, in the VDOS of the nc-Si samples. Figure 5 shows that a reduction in grain size leads to a decrease in this ratio. For nc-Si1, nc-Si8, and nc-Si64, the values of I_{TA}/I_{TO} amount to 0.68, 0.81, and 0.98, respectively. This confirms that the I_{TA}/I_{TO} intensity ratio in the VDOS can be a sensitive probe of the crystalline fraction in nanocrystalline samples. For the sake of comparison, the experimental ratio for nc-Si was found to be 0.88,[43] which is close to the I_{TA}/I_{TO} ratio presently found for the nc-Si8 structure.

IV. MECHANICAL PROPERTIES

During deformation, the average stress is calculated as a function of uniaxial strain (ϵ). The stress-strain curves obtained from the simulations of the bulk SiC and Si samples under uniaxial deformation at 300 K are presented in Fig. 6. We also show in this figure the stress-strain curve of the nanocrystalline sample with an increased number of atoms to investigate the effect of sample size on the deformation response. It is seen that the increase in the number of atoms by a factor of 2 only leads to insignificant changes in the deformation curve. Consequently, the 4096-atom samples used in MD simulations are assumed to be large enough to guarantee meaningful statistics.

The structural and mechanical characteristics of these materials are summarized in Table I.

In the case of the crystalline samples, the sharp bend at a strain $\epsilon_0 \sim 0.4$ in the stress-strain curves points to the brittleness of these crystals. For deformations strictly larger than ϵ_0, an appreciable reduction in the stress is observed. Judging from the character of the stress-strain dependences, one can assume that the 3C-SiC crystal will fail without exhibiting any plasticlike behavior. As for *c*-Si, a weakly noticeable region of plasticlike behavior is observed. We calculated the reversible stress-strain curves for the crystalline and some noncrystalline materials. These curves are shown in Fig. 7. We see that for the 3C-SiC sample, upon release of the stress from the corresponding flow stress, the coincidence between the unloading curves with the loading ones shows that there is no plastic deformation. This suggests that the crystalline material under high-rate uniaxial strains mostly behave elastically until it fails. For *c*-Si, the main peak in the stress-strain curve is not so prominent: consequently, silicon can exhibit weak plasticlike response under uniaxial strain. One important peculiarity should be noted: for the crystalline samples, the stress is not a linear function of the strain inside the elastic region. We do not exclude that this peculiarity can be due to a specificity of the Tersoff potential. To corroborate this finding, experimental results are required. The deformation along the (100) axis of the cubic crystalline samples occurs without any strain hardening, while the deformation along the (110) axis induces strain hardening at strains just below 0.4, which causes a drastic increase in flow stress. We thoroughly examined the atomic configurations of the samples at various stages of the deformation and did not find any structural phase transition. Our investigations were based on analyzing average coordination number, pair-correlation function, and atomic configurations. The results of these investigations prompt us to infer that the aforementioned peculiarities of the behavior of 3C-SiC and *c*-Si under uniaxial tension are caused by the nature of the directionality of the covalent bonds that are strongly anisotropic. Indeed, the anisotropy ratio of a silicon monocrystal under pure elastic deformation is 0.64, which deviates from that of an ideally isotropic material by 36%.[50] This ratio is very close to the ratio between the flow stresses, $\sigma_{flow}(100)/\sigma_{flow}(110) = 0.62$, deduced from deformations of the *c*-Si sample along the (100) and (110) axis (cf. Table I).

Different conclusions will be drawn for the noncrystalline materials. For the nanostructured and amorphous SiC and Si samples, the availability of the amorphous network leads to the appearance of a plastic region. Figure 7 clearly shows that the unloading and loading stress-strain curves coincide, provided the release of the stress is only from the linear region. We also note that the deformation of the nc and *a* systems occurs without hardening. The elastic-plastic response is thought to be the generic mechanical response for materials lacking microstructure or bonding necessary to produce work hardening. In this respect, the mechanical behavior of the noncrystalline bulk SiC and Si structures under uniaxial strain is similar to that of many metallic materials.

As mentioned above, Young's modulus is determined from a strain-stress curve in the linear region that extends to a boundary value called the yield stress. From Fig. 6 and Table I, we see that the lower the yield stress, the higher Young's modulus. In our case, a low value of yield stress is

TABLE I. Structural and mechanical characteristics of *c*-, nc-, and *a*-SiC and Si structures. Notations: a_0, reduced lattice parameter; B, bulk modulus; E, Young's modulus; ν, Poisson's ratio; σ_{yield}, yield stress; σ_{flow}, flow stress. The experimental and theoretical values from other studies are reported in parentheses and curly brackets, respectively. The values of Young's modulus (E_R) and failure strength (σ_{failure}) determined from the rod extension tests are also indicated.

Samples	a_0 (Å)	B (GPa)	E (GPa)	E_R (GPa)	ν	σ_{yield} (GPa)	σ_{flow} (GPa)	σ_{failure} (GPa)
			SiC					
3C-SiC(110)	4.325	224	481	442	0.142	17.8	166.5	88.8
3C-SiC(100)	4.325	224 (224)[a]	481 (468±23)[b]		0.142	17.8	87.8	
nc-SiC1	4.366	216	386	394	0.202	18.6	71.0	77.4
nc-SiC8	4.386	212	363	367	0.215	18.6	68.7	67.8
nc-SiC8(100)	4.370	207	357		0.213	19.7	65.8	
nc-SiC8(110)	4.383	207	394		0.183	18.2	72.6	
nc-SiC64	4.408	200	317	327	0.228	27.6	62.5	59.7
a-SiC	4.402	213 {245}[a]	316 (260–372)[b]	327	0.253	30.6	57.5	57.1
			Si					
c-Si (110)	5.433	97	136	129	0.266	11.7	45.7	36.9
c-Si (100)	5.433	97 (99)[a] {69}[a]	92 (64–166)[a] {74}[c]	90	0.342	13.8	28.5	23.6
nc-Si1	5.434	91	103	104	0.311	13.1	26.2	23.7
nc-Si8	5.439	87	105	110	0.299	12.5	25.2	24.1
nc-Si8(100)	5.435	92	87		0.342	15.6	24.6	
nc-Si8(110)	5.446	91	115		0.289	12.4	29.8	
nc-Si64	5.442	79	95	101	0.300	13.2	23.1	21.2
a-Si	5.525	75 {95}[a]	87	90	0.307	13.2	22.5	19.5

[a]Reference 17 and references therein. The theoretical characteristics were obtained from MD simulations based on the Tersoff potential. The parameters of the C-C potential were determined for graphite.
[b]*a*-SiC films deposited by means of pulsed-laser deposition on Si (100) substrates at deposition temperature ranging from 20 to 650 °C (Ref. 12).
[c]Theoretical values defined from an empirical potential (Ref. 13).

the characteristic feature of a high-strength material. The low values of yield stresses for nanocrystalline structures are a consequence of the deviation from the linear dependence in the elastic region for the corresponding crystals. On the contrary, for many metallic materials, there is a linear dependence between E and σ_Y.[35] In addition, the stress-strain curves were calculated for nc-SiC8 and nc-Si8 samples, with the (100) and (110) crystallite axes aligned along the direction of uniaxial strain. The results are shown in Fig. 8. The flow stress of the (110) oriented nanostructured samples turned out to be the highest among those of other nanostructures. One can see that for nanostructured Si samples, this phenomenon is more prominent. However, in contrast to the crystalline structures, the (110) oriented nanostructured samples do not exhibit strain hardening. In general, the crystallites are randomly oriented in nanostructures. Consequently, the closer the (110) crystallite axis is oriented along

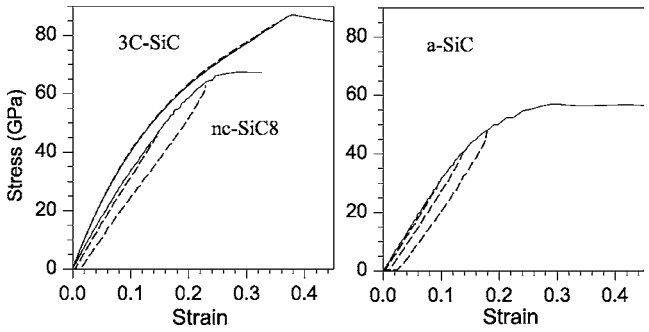

FIG. 7. Stress-strain loading (solid line) and unloading (dashed line) curves for the bulk 3C-SiC, nc-SiC8, and *a*-SiC samples.

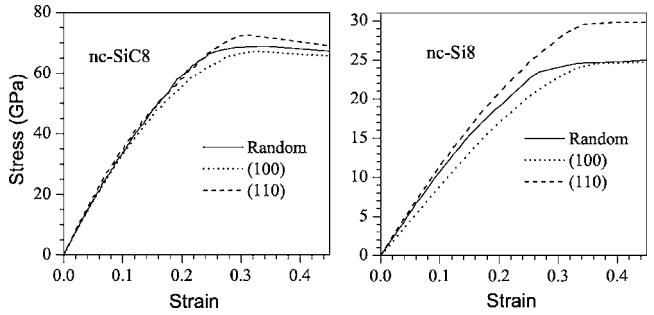

FIG. 8. Stress-strain curves for bulk nc-SiC8 and nc-Si8 samples with different orientations of the crystallites.

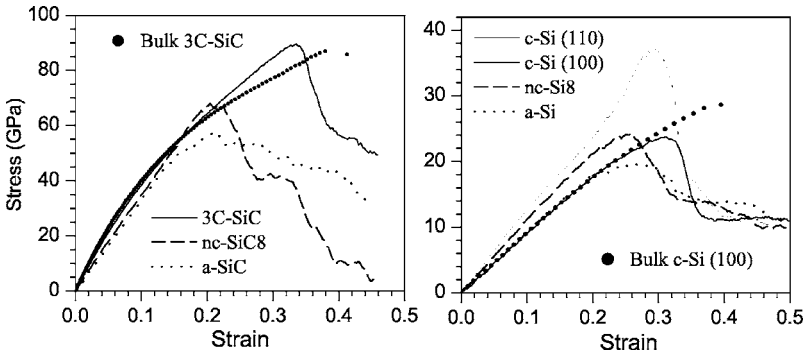

FIG. 9. Stress-strain curves for the SiC and Si structures obtained from the rod-tension tests (v = 100 m/s) and uniaxial strain of the bulk samples.

the strain direction, the higher the strength properties of the samples such is the case for an atomic configuration that is realized in the nc-Si8 sample, where Young's modulus and the flow stress reach maximum values, and the Poison ratio is smaller among all the Si structures. It should be noted that there is a small effect of crystallite orientation on the bulk modulus (cf. Table I). When analyzing the structural dependence of Young's modulus in the case of the SiC nanostructures, one should take into account the structural peculiarities of the amorphous matrix of each nanostructured sample. For nc-SiC1, nc-SiC8, and nc-SiC64, the percentages of Si–Si bonds amount to 14.9%, 15.7%, and 19.5%, while the percentages of Si–C bonds are equal to 73.4%, 72.0%, and 66.0%, respectively. The insignificant increase in the number of C–C bonds (2.8%) does not compensate the overall weakening of the chemical bonding. Therefore, the strengthening of the Si–Si interactions and the weakening of the Si–C interactions along with an increase in the topological disorder of the amorphous matrix with grain size refinement lead to a decrease of E and σ_{flow} and to an increase of ν. It should be noted that, upon reaching σ_{flow}, the stress could not drastically decline because of the infinite sample size generated by the PBC. Therefore, the bulk samples exhibit a plastic plateaulike region around the flow stress values. As will be shown below, the flow stress for the bulk samples is associated with the failure strength of the rodlike samples.

Figure 9 shows the stress-strain dependences of the SiC and Si structures obtained from the rod extension tests. First of all, we note that the two approaches discussed for the mechanical tests of our samples give very similar results. In particular, Young's moduli and failure strengths determined from the two tests are in good agreement. There is only one difference: the curves presented in Fig. 9 do not have any plastic plateaulike region. The sample under rod extension is destroyed when the internal stress reaches a maximum (cf. Fig. 3).

So far, we investigated the strength properties of the SiC and Si rods that undergo extension with a constant rate of 100 m/s. To clarify the effect of extension rate on Young's modulus and failure strength, we carried out MD simulations of the rod extension with different rates, v=2, 50, and 100 m/s, using a time step of 2.5 fs. In Fig. 10, we show the strain-stress curves for the SiC and Si rodlike samples defined at various extension rates. For the 3C-SiC sample, the brittle failure is observed. However, for the c-Si structure, there is a weakly noticeable region of plastic behavior. So, as mentioned above, this material is supposed to possess weakly expressed microplasticity. The character of plastic behavior of the amorphous samples is weakly influenced by v. One can see that the failure strength of all the samples is very sensitive to v. The higher v is, the higher σ_{failure} is. In many instances, it is this effect that is observed in corresponding experiments. The Young's modulus of the crystalline samples weakly depends on extension rate, whereas, for the noncrystalline SiC structures, it slightly increases with v.

Based on the calculated stress-strain relationships, we now attempt to estimate the nanohardness (H) of some structures under investigation. It is known that the ratio of the maximum load to the surface area in the plastic regime is related to the hardness. In our case, the failure strength is related to the nanohardness of the SiC and Si structures.[15] Taking into account the fact that nanoindentation is generally carried out with rates of several nm/s, and keeping in mind that σ_{failure} depends on v, we have extrapolated $\sigma_{\text{failure}}(v)$

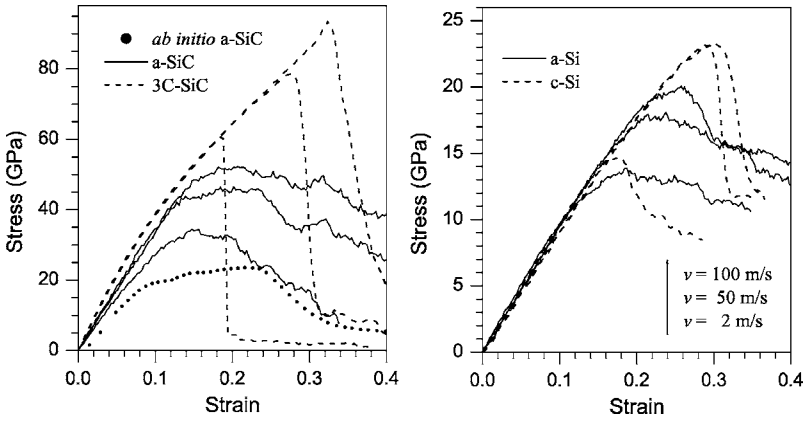

FIG. 10. Stress-strain curves for the SiC and Si structures obtained from rod-tension tests at various extension rates: 2, 50, and 100 m/s. The failure strength increases with the extension rate. The time step used in MD simulations amounts to 2.5 fs. The data of the first-principles MD simulations for a 128-atom a-SiC sample are also shown (Ref. 15).

when $v \to 0$. We predict the following values of nanohardness for 3C-SiC, 60.1 (42); nc-SiC8, 36.1; *a*-SiC, 34.2 (24–48); *c*-Si, 15.7 (11–14); nc-Si8, 18.5; *a*-Si, 13.9 GPa. In parentheses, the corresponding experimental values[3,6,12,13] are presented. For the sake of comparison, the nanohardness values of 3C-SiC, nc-SiC, and *a*-SiC determined from MD simulations of nanoindentation[31] were 77, 39, and 30 GPa, respectively. Based on the first-principles MD simulations of a 128-atom sample of *a*-SiC subjected to uniaxial strain, Galli *et al.*[15] predict $H=24$ GPa. We see that, for *a*-SiC, the theoretical values of H are in rather good agreement with those measured in nanoindentation experiment. As expected, the modified Tersoff potential overestimates H for the crystalline materials; however, it predicts values of nanohardness with higher degree of certainty as compared to other theoretical procedures.[15,31] In Fig. 10, we show the results of comparison between our data and the results of first-principles MD simulations of *a*-SiC.[15] Up to the failure region, the intrinsic stress of our sample is higher than that of the first-principles structure, which can be assigned to an overestimation of stress state of the material with the Tersoff potential. However, allowing for the fact that the first-principles nanohardness is lower than the experimental values, most likely such a discrepancy is due to the specific conditions of first-principles MD simulations.[15] In Table I, we also summarize the available experimental and theoretical values of B and E for the systems under investigation. The rather good agreement between the calculated and experimental characteristics is observed although, in the case of the Si structures, our approach slightly underestimates Young's modulus compared to the experimental values.

V. STRUCTURAL CHANGES

We examined the atomic configurations of the bulk sample during an uniaxial strain. The crystalline materials preserve their fourfold coordination up to the flow stress values (not shown). Beyond these values, the crystalline network drastically transforms into an amorphous matrix. The randomization begins from the edge of the samples and rapidly spreads towards the center.

By analyzing the atomic structure of the bulk nc-SiC8 and *a*-SiC samples under uniaxial strain, it was established that the elastic behavior is determined by modifications in the tetrahedral network. The correlation between the percentage of nontetrahedrally coordinated atoms ($\Delta N4$) and the stress-strain dependences of the nc-SiC8 and *a*-SiC samples is shown in Fig. 11. We see that the flat region in the $\Delta N4(\epsilon)$ curves corresponds to a region of elastic deformation. The onset of plastic deformation is accompanied by a drastic reduction in the number of tetrahedrally coordinated atoms.

Figure 12 displays the pair-correlation function of the bulk nc-SiC8 and nc-Si8 samples under different stages of uniaxial strain. An analysis of the pair correlations and the atomic configurations (cf. Fig. 3) shows that, during the uniaxial tension, the deformation of both grains and amorphous matrix is observed. The grains preserve the crystalline configurations even at high strains. However, upon reaching the plateaulike region, their structure gradually transforms into an amorphous matrix, which is mostly caused by amorphization of the grain boundaries. The grains fail during plastic deformation nonsimultaneously, i.e., the closer the (110) grain axis to the direction of deformation, the higher the grain stability. The peaks associated with nearest-neighbor

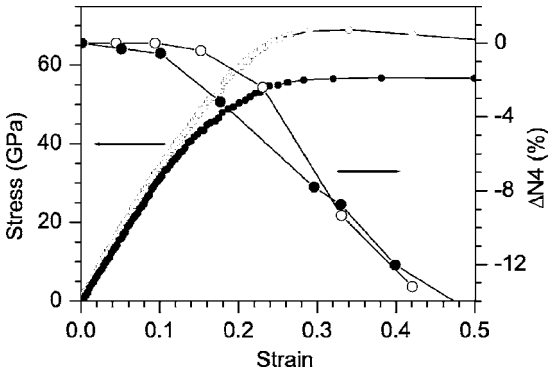

FIG. 11. Correlations between stress behavior and change in the number of fourfold coordinated atoms ($\Delta N4$) for the nc-SiC8 (open circles) and *a*-SiC (full circles) samples under (100) uniaxial deformation.

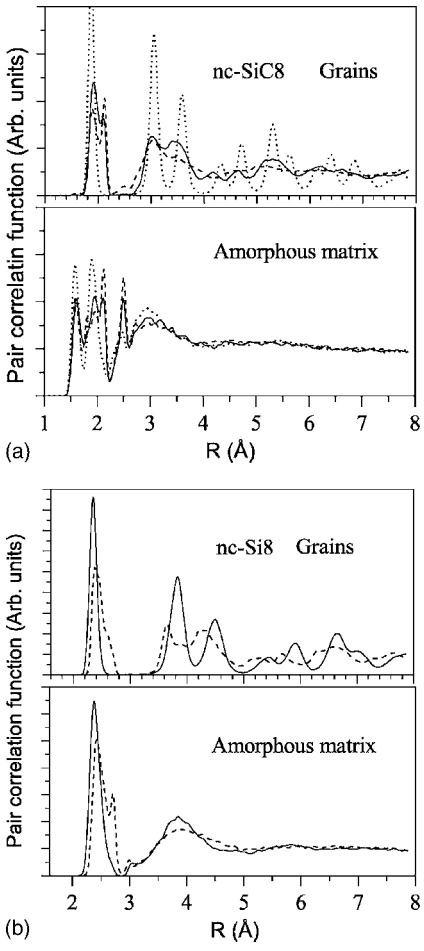

FIG. 12. Pair-correlation function (PCF) of the bulk nc-SiC8 and nc-Si8 samples under different stages of uniaxial strain. nc-SiC8: $\epsilon=0$ (dotted line), $\epsilon=0.23$ (solid line), and $\epsilon=0.42$ (dashed line); nc-Si8: $\epsilon=0$ (solid line) and $\epsilon=0.309$ (dashed line).

interactions in the PCF related to the grains and the amorphous matrix split, which causes the anisotropy of the stress fields. For the SiC samples, comparison of the stress-strain curves between the crystalline and amorphous samples shows that the main anisotropic stress is accumulated within the grains. This explains why Young's modulus of *a*-SiC is smaller, although the bulk modulus of the amorphous sample is higher when compared with those of the nc-SiC8 and nc-SiC64 samples. In the sequence "nc1-nc8-nc64-*a*," the percentages of Si–Si bonds in the amorphous matrix were found to be 28.6%, 30.2%, 37.5%, and 30.0%, respectively. Taking into account the fact that the crystalline fraction is the same for all nc-SiC samples, one concludes that the observed changes in the bulk modulus for the above sequence correlates fairly well with the changes in the percentage of Si–Si bonds in the amorphous matrix (cf. Table I). In contrast to the SiC systems, the Si structures are homopolar, and an increase in randomization of the amorphous network in the sequence of "nc1-nc8-nc64-*a*" only causes a gradual reduction of the bulk modulus.

VI. CONCLUSIONS

Molecular-dynamics simulations have been used to study atomic structures, vibrational spectra, and strength properties of crystalline, nanocrystalline, and amorphous SiC and Si. The nanostructured materials were represented by sphericallike randomly oriented crystallites embedded in an amorphous matrix. The initial nanocrystalline fraction was approximately 50% for all nanostructured samples. The SiC nanostructures had 3C-SiC crystallites of 3.5 (nc-SiC1), 1.8 (nc-SiC8), and 0.9 nm (nc-SiC64) in diameter, and the Si nanostructures had *c*-Si crystallites of 4.3 (nc-Si1), 2.2 (nc-Si8) and 1.1 nm (nc-Si64) in diameter. Despite the same crystalline fraction in nc-SiC samples, the homopolar Si-Si interactions strengthen with grain size refinement. In *a*-SiC, the different types of bonds are equally present.

The vibrational spectra of the SiC and Si samples have a four-peak structure with one prominent peak associated with the TO vibrations at $\sim 810\ \mathrm{cm}^{-1}$ (SiC structures) and $\sim 570\ \mathrm{cm}^{-1}$ (Si structures). Towards full amorphization, an increase in the topological disorder of the amorphous matrix and a decrease in chemical order lead to a shift of these peaks towards smaller wave numbers and to a decrease in their intensity.

The comprehensive investigations of the strength properties of the SiC and Si structures under uniaxial strain with and without periodic boundary constraints enabled us to arrive at the following conclusions.

(1) The 3C-SiC sample behaves elastically until they fail, whereas for *c*-Si, a small plasticlike region is observed. The stress of these materials is not a linear function of the strain inside the elastic region. The deformation along the (100) axis of the SiC and Si crystalline structures occurs without any strain hardening, while deformation along the (110) axis induces significant strain hardening.

(2) The calculations for the nanostructured samples in which the (100) and (110) crystallite axis are aligned along the strain direction indicate an enhancement of the strength properties of the structures with the (110) crystallite orientation. Among all the noncrystalline samples studied, an enhancement in the strength properties of nc-Si8 was observed, which is caused by an optimal crystallite orientation.

(3) In the sequence "nc-SiC1–nc-SiC8–nc-SiC64–*a*-SiC," an enhancement of the Si-Si bonding and disorder leads to a decrease in Young's modulus and failure strength and to a increase in Poisson's ratio. For heteropolar-bonded materials, such as nc-SiC and *a*-SiC, chemical order is a more important factor than crystallite orientation: changes in chemical order alone mostly determine the strength properties of the SiC nanostructures.

(4) The two mechanical tests performed on the SiC and Si samples with and without taking into account PBC provide similar results. Young's moduli and failure strengths determined from the two tests are in good agreement. There is only one essential difference: the simulation with PBC gives stress-strain curves with a plastic plateaulike region, not observed in the case of the simulation without PBC (rod extension). In the latter case, the samples failed when the internal stress reached a maximum value (failure strength).

(5) The failure strength of all the samples increases with extension rate. Young's modulus of the crystalline materials is practically independent of the extension rate v, whereas, for the noncrystalline structures, it slightly decreases with a decrease in extension rate.

(6) The rather good agreement noted between the calculated and the experimental characteristics confirms that our theoretical procedure is able to reproduce the experimental strength properties with acceptable accuracy. It predicts the mechanical properties of the SiC and Si structures, which are in reasonable agreement with those determined with other MD computational schemes. The main shortcoming of the procedure consists in an overestimation of the failure strength of the crystalline SiC and Si.

ACKNOWLEDGMENTS

This work was supported in part by the CRDF Contract No. UK-E2-2589-KV-04. The work of P.T. was performed under the auspices of the U.S. Department of Energy by the University of California Lawrence Livermore National Laboratory under Contract No. W-7405-ENG-48. The authors thank A. Gonis for a careful reading of the manuscript.

[1] J. Kanicki, *Amorphous and Microcrystalline Semiconductor Devices* (Artech House, Boston, 1991), Vol. I and II.
[2] R. Rizzoli, R. Galloni, C. Summonte, F. Demichelis, C. F. Pirri, E. Tresso, G. Crovini, F. Giorgis, P. Rava, and A. Madan, in *Amorphaus Silicon Technology*, edited by H. Hack, P. A. Schiff, A. Madou, M. Powell, and A. Matsuda, MRS Symposia Proceedings No. 377 (Materials Research Society, Pittsburgh, 1995), p. 909.
[3] *Amorphous and Crystalline Silicon Carbide: Materials and Applications*, Proceedings of the E-MRS, edited by L. Calcagno, A. Hallen, R. Martins, and W. Skorupa (Elsevier, Amsterdam, 2001), p. 528.
[4] J. Esteve, A. Lousa, E. Martinez, H. Huck, E. B. Halac, and M. Reinoso, Diamond Relat. Mater. **10**, 1053 (2001).
[5] O. K. Porada, V. I. Ivashchenko, L. A. Ivashchenko, G. V. Rusakov, S. N. Dub, and A. I. Stegnij, Surf. Coat. Technol. **180-181**, 122 (2004).
[6] S. Sundararajan and B. Bhushan, in *Proceedings of the Second World Tribology Congress*, edited by F. Franek, W. J. Bartz, and A. Pauschitz (The Austrian Tribology Society, Vienna, 2001), pp. 347–359.
[7] M. J. Loboda and M. K. Ferber, J. Mater. Res. **8**, 2908 (1993).
[8] M. A. Bayne, Z. Kurokawa, N. U. Okorie, B. D. Roe, L. Johnson, and R. W. Moss, Thin Solid Films **107**, 201 (1983).
[9] J. M. Grow, in *Thin Films: Stresses and Mechanical Properties IV*, edited by P. H. Tawnsend, T. P. Weihs, J. B. Sanchez, Jr., and P. Borgesen, MRS Symposia Proceedings No. 308 (Materials Research Society, Pittsburgh 1993), p. 601.
[10] H. Kung, T. R. Jervis, J. P. Hirvonen, J. D. Embury, T. E. Mitchell, and M. Nastasi, Philos. Mag. A **71**, 759 (1995).
[11] M. A. El. Khakani, M. Chaker, A. Jean, S. Boily, J. C. Kiffer, M. E. O'Hern, M. F. Ravet, and F. Rousseaux, J. Mater. Res. **9**, 96 (1994).
[12] M. A. El. Khakani, M. Chaker, M. E. O'Hern, and W. C. Oliver, J. Appl. Phys. **82**, 4310 (1997).
[13] *High-Pressure Surface Science and Engineering*, edited by Y. Gogotsi and V. Domnich (IOP, Bristol, 2004).
[14] F. Finocchi, G. Galli, M. Parrinello, and C. M. Bertoni, Phys. Rev. Lett. **68**, 3044 (1992).
[15] G. Galli, F. Gygi, and A. Catellani, Phys. Rev. Lett. **82**, 3476 (1999).
[16] J. Tersoff, Phys. Rev. B **49**, 16349 (1994).
[17] P. C. Kelires, Phys. Rev. B **46**, 10048 (1992).
[18] V. I. Ivashchenko, P. E. A. Turchi, V. I. Shevchenko, L. A. Ivashchenko, and G. V. Rusakov, Phys. Rev. B **66**, 195201 (2002).
[19] M. Ishimaru, J. Appl. Phys. **91**, 686 (2002).
[20] P. M. Voyles, N. Zotov, S. M. Nakhmanson, D. A. Drabold, J. M. Gibson, M. M. J. Treacy, and P. Keblinski, J. Appl. Phys. **90**, 4437 (2001).
[21] S. M. Nakhmanson, P. M. Voyles, N. Mousseau, G. T. Barkema, and D. A. Drabold, Phys. Rev. B **63**, 235207 (2001).
[22] M. Durandurdu and D. A. Drabold, Phys. Rev. B **66**, 205204 (2002).
[23] S. V. Khare, S. M. Nakhmanson, P. M. Voyles, P. Keblinski, and J. R. Abelson, Appl. Phys. Lett. **85**, 745 (2004).
[24] H. Balamane, T. Halicioglu, and W. A. Tiller, Phys. Rev. B **46**, 2250 (1992).
[25] J. Tersoff, Phys. Rev. B **39**, 5566 (1989).
[26] E. Pearson, T. Takai, T. Hilicioglu, and W. A. Tiller, J. Cryst. Growth **70**, 33 (1984).
[27] M. Tang and S. Yip, J. Appl. Phys. **76**, 2719 (1994).
[28] M. Tang and S. Yip, Phys. Rev. B **52**, 15150 (1995).
[29] F. Gao and W. J. Weber, Phys. Rev. B **63**, 054101 (2000).
[30] F. Shimojo, I. Ebbsjo, R. K. Kalia, A. Nakano, J. P. Rino, and P. Vashishta, Phys. Rev. Lett. **84**, 3338 (2000).
[31] I. Szlufarska, Mater. Today **9**, 42 (2006).
[32] P. I. Rovira and F. Alvarez, Phys. Rev. B **55**, 4426 (1997).
[33] Z. Li and R. C. Bradt, J. Mater. Sci. **21**, 4366 (1986).
[34] F. D. Murnaghan, Proc. Natl. Acad. Sci. U.S.A. **30**, 244 (1944).
[35] J. Schiotz, T. Vegge, F. D. Di Tolla, and K. W. Jacobsen, Phys. Rev. B **60**, 11971 (1999).
[36] M. J. Mehl, Phys. Rev. B **47**, 2493 (1993).
[37] P. Blaha, K. Schwartz, P. Sorantin, and S. Tricky, Comput. Phys. Commun. **597**, 399 (1990).
[38] J. P. Perdew, K. Burke, and M. Ernzerhof, Phys. Rev. Lett. **77**, 3865 (1996).
[39] P. E. Blochl, O. Jepsen, and O. K. Andersen, Phys. Rev. B **49**, 16223 (1994).
[40] M. Ishimaru, I.-T. Bae, Y. Hirotsu, S. Matsumura, and K. E. Sickafus, Phys. Rev. Lett. **89**, 055502 (2002).
[41] K. Laaziri, S. Kycia, S. Roorda, M. Chicoine, J. L. Robertson, J. Wang, and S. C. Moss, Phys. Rev. B **60**, 13520 (1999).
[42] H. Bilz and W. Kress, *Phonon Dispersion Relations in Insulators* (Springer-Verlag, Berlin, 1979).
[43] W. A. Kamitakahara, C. M. Soukoulis, H. R. Shanks, U. Buchenau, and G. S. Grest, Phys. Rev. B **36**, 6539 (1987).
[44] J. C. Burton, L. Sun, M. Pophristic, S. J. Lukacs, and F. H. Long, J. Appl. Phys. **84**, 6268 (1998).
[45] M. B. Yu, Rasli, S. F. Yoon, Z. M. Chen, J. Ahn, Q. Zhang, K. Chew, and J. Cui, J. Appl. Phys. **87**, 8155 (2000).
[46] M. B. Yu, Rasli, S. F. Yoon, S. J. Xu, K. Chew, J. Cui, J. Ahn, and Q. Zhang, Thin Solid Films **377-378**, 177 (2000).
[47] F. Giorgis, A. Chiodini, G. Cicero, S. Ferrero, P. Mandracci, G. Barucca, R. Reitano, and P. Musumeci, Diamond Relat. Mater. **10**, 1264 (2001).
[48] N. A. E. Forhan, M. C. A. Fantini, and I. Pereyra, J. Non-Cryst. Solids **338-340**, 119 (2004).
[49] M. Ishimaru, M. Yamaguchi, and Y. Hirotsu, Phys. Rev. B **68**, 235207 (2003).
[50] T. H. Courthey, *Mechanical Behavior of Materials* (McGraw-Hill, Singapore, 1990), p. 59.